Supplemental Material: Size effects on the thermal conductivity of amorphous silicon thin films

Jeffrey L. Braun[1], Christopher H. Baker[1], Ashutosh Giri[1], Mirza Elahi[2], Kateryna Artyushkova[3], Thomas E. Beechem[4], Pamela M. Norris[1], Zayd C. Leseman[5], John T. Gaskins[1], and Patrick E. Hopkins[1]

[1]*Department of Mechanical and Aerospace Engineering, University of Virginia, Charlottesville, VA 22904, USA*
[2]*Department of Electrical and Computer Engineering, University of New Mexico, Albuquerque, NM 87131, USA*
[3]*Department of Chemical and Nuclear Engineering, University of New Mexico, Albuquerque, NM 87131, USA*
[4]*Sandia National Laboratories, Albuquerque, NM 87123, USA*
[5]*Department of Mechanical Engineering and Manufacturing Training and Technology Center, University of New Mexico, Albuquerque, NM 87131, USA*

Sample Preparation

RF sputter deposition was used to fabricate the a-Si thin films used in this study. The films vary in thickness from 2 – 1632 nm and were all deposited on silicon substrates. The fabrication process involved patterning of a silicon wafer by photolithography process, deposition of amorphous Si thin film with RF sputtering, lift-off process to get precise measurement for the film thickness, and e-beam deposition of aluminum on top of the thin film. This aluminum layer acts as an opto-thermal transducer in our TDTR procedure. The thicknesses of the a-Si films were varied by the deposition time of the RF sputtering and measured with a profilometer. The RF sputtering was carried out with a RF source (13.56 MHz) instead of DC source to avoid charge build up in the thin film. After the entire chamber was pumped down to the pressure of 10^{-6} Torr, the sputtering conditions were maintained with 3 mTorr carrier gas pressure of Ar and gun power of 300 W to sustain the plasma for a certain period of deposition time. The intrinsic target Si was used to avoid any type of doping incorporation in the thin film, which can change the characteristics of the thermal properties of interest.

Aluminum was deposited on top of the a-Si by e-beam evaporation. The chamber was pumped down to a base pressure of $2\text{x}10^{-6}$ Torr and at a voltage of 10 kV, e-beam current was increased at a rate of 10 mA/min to reach 160

Table S1: Elemental composition and Si speciation for old and new samples before and after cleaning with Ar^+ ion beam

Sample Type	C 1s %	O 1s %	Si 2p %	C thickness (nm)	Si %	SiO_X %	SiO_2%
Sample uncleaned	56.9	12.0	31.1	2.9	79.8	13.7	6.5
Sample cleaned	22.5	4.4	73.1	0.9	78.8	20.9	0.3

mA. The shutter between the source and the sample was then opened to allow a deposition rate of 2 Å/s. Average Al thickness deposited was 80.72 nm as measured with profilometry. Using the decay signal in our TDTR measurements within a picosecond acoustics regime, we verify this thickness to within ±3 nm.

Sample Characterization

All a-Si samples were characterized using X-ray photoemission spectroscopy (XPS). XPS spectra were acquired by a Kratos AXIS DLD Ultra photoelectron spectrometer using a monochromatic Al Kα source operating at 225 W. Charge compensation was accomplished using low energy electrons. Samples were analyzed at 90° take-off angles (8 - 10 nm depth). Survey spectra of each area were completed first at 80 eV pass energy for 4 min. High-resolution spectra of C 1s, O 1s and Si 2p were then acquired at pass energy of 20 eV for 6 min. Linear background was used for elemental quantification of C 1s, N 1s, O 1s and Si 2p spectra. Quantitative analysis is based on sensitivity factors provided by the manufacturer. All spectra were charge referenced to the aliphatic carbon at 284.8 eV. Curve fitting analysis was carried out using individual peaks of constrained width, position, and 70 % Gaussian/30% Lorentzian line shape. Three areas per sample were analyzed.

The Ar^+ ion gun on the Kratos AXIS Ultra photoelectron spectrometer was used as the argon beam source for cleaning top layers of the sample. The 2 cm x 2 cm areas on the samples were sputtered with a 5 keV Ar ion beam operating at 25 mA emission current for 3 minutes each. Small area 100 micron C 1s, O 1s and S 2p high resolution spectra were acquired from the sputtered areas for 15 minutes at 20 eV pass energy. Table 1 shows the elemental composition and Si speciation for the samples before and after cleaning with Ar^+ ion beam. The pristine surfaces contain a large amount of carbon at 57 %. After ion beam sputtering approximately 1 nm of carbon overlayer is still retained.

Pristine samples differ in the chemical environment significantly. After cleaning the surface with ion beam, the chemistry of the samples changed slightly as silica was completely removed, but silicon oxide was still a significant component of the surface.

Raman spectroscopy was used to confirm the amorphous nature of the films and assess the presence of oxygen that may have evolved with oxidation. To this end, Raman spectra were acquired using a Witec alpha300R Raman system implementing 532 nm light and a 100x/0.95 objective. Powers were kept below 0.5 mW to minimize heating and curb any laser-induced damage. Shown in Figure S1 are average spectra acquired on a-Si films and that of a film of SiO_2. For both spectra, the narrow band at ∼520 cm^{-1} characteristic of the triply degenerate optical phonons at the Γ point of the Brillouin in crystalline silicon is absent. Crystalline silicon is therefore not present in the films.

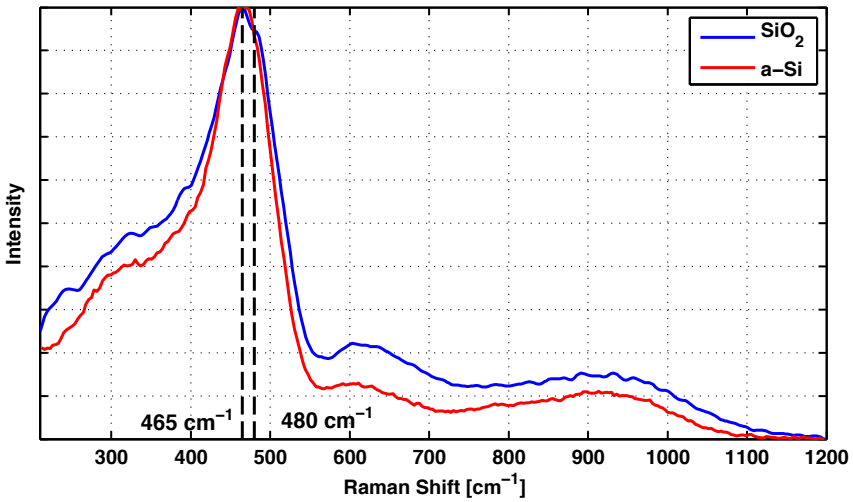

Figure S1: Normalized Raman spectra of thin films of amorphous Si and that of SiO_2

The Raman spectra between the a-Si film and that of SiO_2 are extremely similar having a major band near 465 cm^{-1} and an additional feature at ~605 cm^{-1}. In the case of SiO_2, the most prominent mode is expected in the 450 - 460 cm^{-1} spectral window and is correlated with the vibration of 6-member rings [1, 2]. The mode at ~605 cm^{-1} has been ascribed to a defect mode in SiO_2 [3]. For a-Si, meanwhile, a prominent mode is expected at ~480 cm^{-1} [4, 5, 6, 7] with stretching and "wagging" modes at ~600 and 900 cm^{-1} that arise with the interaction between the silicon matrix and hydrogen present in the material [5]. Taken together, the heuristic typically employed for the differentiation of a-Si and that of SiO_2 is the position of the main peak where a feature located near 460 cm^{-1} is assigned to SiO_2 and that near 480 cm^{-1} is attributed to a-Si [7]. Peak position based material discrimination is to be approached with caution, however, as strain can shift the position of a peak thereby "fooling" the heuristic. For instance, Sato et al. [1] provide a Raman spectrum of SiO_2 with a peak position near 480 cm^{-1} whereas Lannin et al. reported an a-Si signal having a main feature near 460 cm^{-1} [8]. Taken together, Raman is therefore only able to confirm the lack of crystalline Si but is not able to assess the level of oxidation in the films.

Sensitivity Analysis

We quantify the level of sensitivity to a specific parameter using the approach given by Costescu et al. [9], in which we take the partial derivative of the calculated measured signal (ratio, X, Y, magnitude, or phase) with respect to the parameter of interest. For instance, the sensitivity of a ratio measurement to thermal conductivity of the a-Si layer would be calculated via:

$$S_{\kappa_{a-Si}} = \frac{\partial(-V_{in}/V_{out})}{\partial(\kappa_{a-Si})} \tag{S1}$$

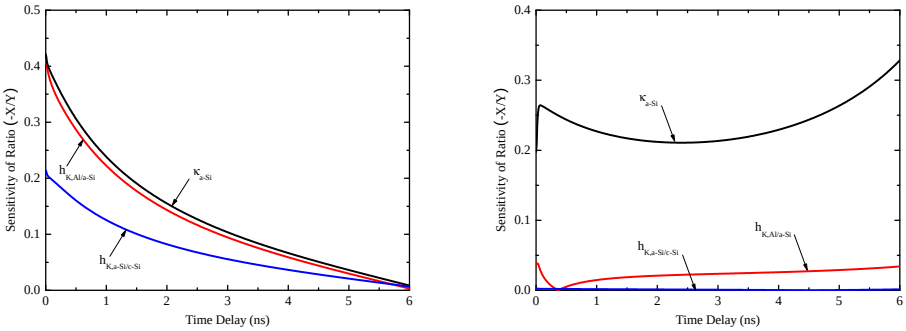

(a) 10 nm a-Si Sensitivity

(b) 200 nm a-Si Sensitivity

Figure S2: Sensitivity of calculated ratio of measured signal on a 10 nm a-Si film thickness sample (a) and 200 nm a-Si film thickness sample (b) to $h_{\mathrm{K,a-Si/Si}}$, $h_{\mathrm{K,Al/a-Si}}$, and $\kappa_{\mathrm{a-Si}}$.

where V_{in} is the in-phase component of the measured signal from the lock-in amplifier and V_{out} is the out-of-phase component. For example, Figure S2 shows the sensitivity analysis for a 10 nm and a 200 nm thick a-Si thickness sample, where the absolute value is taken to compare magnitures of influence among parameters. Note that for the 200 nm sample In this case, the relative magnitude of $h_{\mathrm{K,a-Si/Si}}$ is insignificant compared to that of both $h_{\mathrm{K,Al/a-Si}}$ and $\kappa_{\mathrm{a-Si}}$, meaning we can analyze our data based on these latter two parameters alone. By comparison, films with thicknesses of the 10 nm a-Si film sample shows significant sensitivity to $h_{\mathrm{K,a-Si/c-Si}}$. To understand at what thickness we become insensitive to $h_{\mathrm{K,a-Si/c-Si}}$, we apply this sensitivity analysis procedure for a range of films thicknesses and average the magnitude of sensitivity over the time regime of interest (200ps - 5.5 ns) to construct a sensitivity vs. a-Si film thickness relation, shown in Figure S3. Based on this analysis, sensitivity to $h_{\mathrm{K,a-Si/c-Si}}$ becomes negligible for a-Si film thicknesses greater than approximately 150 nm.

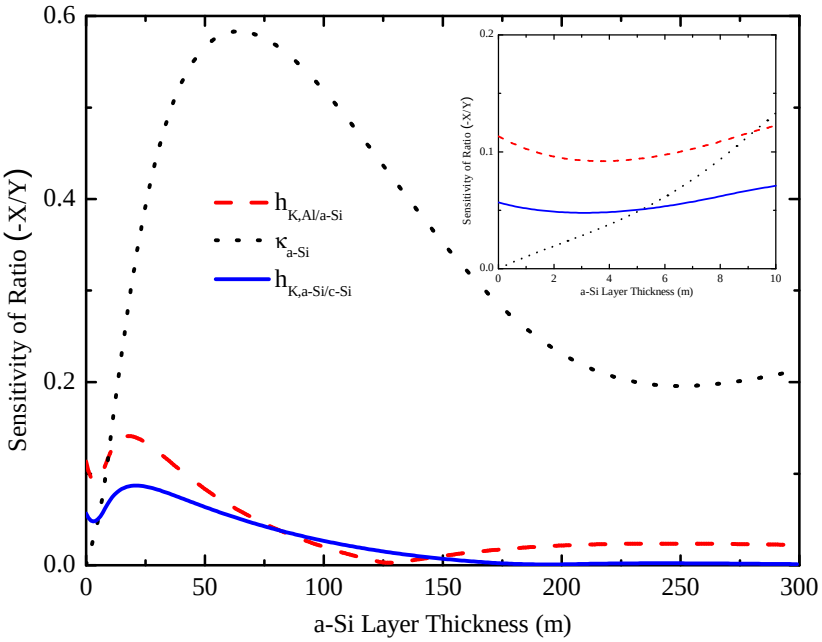

Figure S3: Sensitivity vs. a-Si film thickness for film thicknesses ranging from 0 to 300 nm. The inset shows the same data plotted for film thicknesses ranging from 0 to 10 nm.

TDTR Analysis

We analyzed the TDTR ratio data by analyzing the thin film samples (a-Si thicknesses for which there is sensitivity to the a-Si/c-Si interface) by treating the a-Si layer as an interface and fitting for the total conductance ($h_{K,interface} = U_m$) and the thermal conductivity of the c-Si substrate (κ_{c-Si}). For samples characterized by having a semi-infinite a-Si film (a-Si film thicknesses for which there is no sensitivity to the a-Si/c-Si interface), we fit for the thermal boundary conductance between the aluminum transducer and the a-Si film ($h_{K,Al/a-Si}$) and the a-Si thermal conductivity. Figure S4 shows characteristic data and fits for thin-film analysis (14 nm a-Si) and a semi-infinite film analysis (578 nm a-Si).

We note that the thermal conductivity measured in the thicker samples, characterized as "semi-infinite" for modulation frequency of 12.2 MHz, is independent of modulation frequency (and therefore, thermal penetration depth). Indeed, Figure S5 illustrates this for a sample with a-Si film thickness of 454 nm and 578 nm. In both cases, the thermal penetration depth goes beyond the a-Si thickness, yet thermal conductivity remains constant (within experimental uncertainty). TDTR is an effective measure of the thermal conductivity of high thermal effusivity materials when the material is semi-infinite and the thermal

penetration depth is relatively small; thus this thermal penetration depth independence is expected. Moreover, together with the fact that our heater diameter is 55 microns (ensuring one-dimensional heat conduction), this implies that any size effects on the thermal conductivity among samples can be attributed to differences in film thickness rather than any experimental length scales.

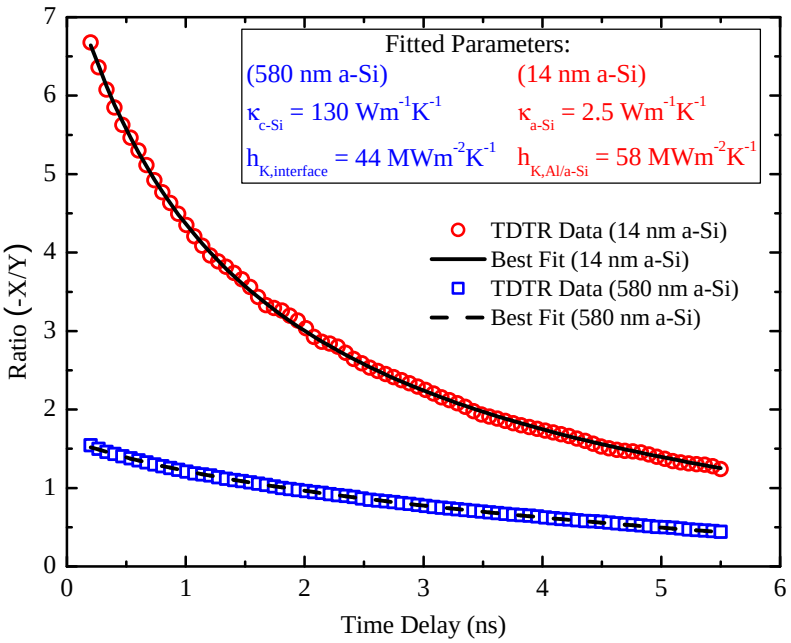

Figure S4: Representative TDTR data for a thin film sample (a-Si film thickness of 14 nm) and a semi-infinite sample (a-Si film thickness of 578 nm)

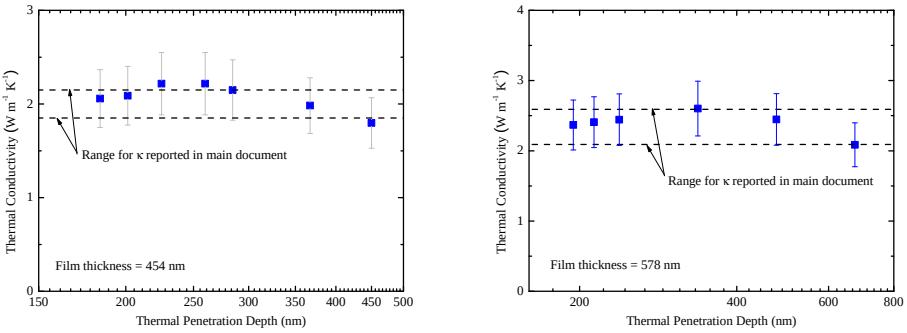

Figure S5: Thermal conductivity vs. thermal penetration depth for a-Si film of thickness 454 nm (left) and 578 nm (right).

Series Resisor Model

We use a series resistor model to determine the intrinsic thermal conductivity of our thin film samples given by:

$$\frac{1}{U_m} = \frac{1}{h_{\mathrm{K,total}}} + \frac{d}{\kappa_i} \tag{S2}$$

where U_m is the total measured thermal conductance across the Al/a-Si interface, a-Si layer, and a-Si/Si interface, κ_i is the intrinsic thermal conductivity h_{total} accounts for the both $h_{\mathrm{Al/a-Si}}$ and $h_{\mathrm{a-Si/Si}}$ via:

$$\frac{1}{h_{\mathrm{K,total}}} = \frac{1}{h_{\mathrm{Al/a-Si}}} + \frac{1}{h_{\mathrm{a-Si/c-Si}}} \tag{S3}$$

Solving for κ_i in Eq. S2, we find:

$$\kappa_i = \left(\frac{1}{U_m} - \frac{1}{h_{\mathrm{K,total}}}\right)^{-1} d = \frac{U_m d h_{\mathrm{K,total}}}{h_{\mathrm{K,total}} - U_m} \tag{S4}$$

Defining the effective thermal conductivity, κ_{eff}, as $\kappa_{\mathrm{eff}} = U_m d$, we write:

$$\kappa_i = \frac{\kappa_{\mathrm{eff}} h_{\mathrm{K,total}}}{h_{\mathrm{K,total}} - \frac{\kappa_{\mathrm{eff}}}{d}} = \frac{\kappa_{\mathrm{eff}}}{1 - \frac{\kappa_{\mathrm{eff}}}{d h_{\mathrm{K,total}}}} \tag{S5}$$

which is in agreement with the model given by [10]. Using Eq. S5, we fit κ_i and $h_{\mathrm{K,total}}$ to our experimental data using nonlinear least-squares fit. The best fit value for κ_i is ∼1.1 W m^{-1} K $^{-1}$ (with 95% confidence bounds of 0.9549 – 1.21 W m^{-1} K $^{-1}$) while the best fit value for $h_{\mathrm{K,total}}$ is ∼91.6 MW m^{-2} K $^{-1}$ (with 95% confidence bounds of 61.72 – 121.5 MW m^{-2} K $^{-1}$). To systematically study the range of thicknesses for which this procedure is appropriate, we apply this fitting procedure using all possible combinations of data in this thin film regime ($\sum_{i=2}^{5} \binom{6}{i} = 57$ combinations of data points). The average value for our best fit is $\kappa_i = 1.1$ W m^{-1} K $^{-1}$ with a standard deviation of 0.11 W m^{-1} K $^{-1}$ and $h_{\mathrm{K,total}} = 94$ MW m^{-2} K $^{-1}$ with a standard deviation of 16 MW m^{-2} K $^{-1}$.

The only outlier to this best fit value for thermal conductivity came for the combination of 3 and 7 nm films, for which $\kappa_i = 1.6$ W m^{-1} K^{-1} and $h_{\mathrm{K,total}} =$ 87 MW m^{-2} K^{-1} . While this may suggest the assumption of constant thermal conductivity fails for these films, it is not possible to draw a solid conclusion. This discrepancy may be a result of the very narrow range (film thicknesses only separated by 4 nm) over which to fit. Moreover, the sensitivity to $h_{\mathrm{K,total}}$ in this regime is extremely high, meaning that any fluctuations to this value will drastically influence the fitted value for κ_i. Indeed, the fitted value $h_{\mathrm{K,total}}$ is within a standard deviation of the mean of all fitted $h_{\mathrm{K,total}}$, κ_i, yet κ_i as fitted is almost five standard deviations above the mean for all κ_i. Removing these two data points does not significantly influence the results; we calculate $\kappa_i = 1.12$ W m^{-1} K^{-1} and $h_{\mathrm{K,total}} = 82$ MW m^{-2} K^{-1}, shifting our derived thermal conductivities up in magnitude only 5%.

Using the same procedure on our a-SiO_2 films, we find the best fit value for κ_i is ∼1.4 W m^{-1} K^{-1} (with 95% confidence bounds of 1.2802 – 1.526 W m^{-1} K^{-1}) while the best fit value for $h_{\mathrm{K,total}}$ is ∼180 MW m^{-2} K^{-1} (with 95% confidence bounds of 124.9 – 135.4 MW m^{-2} K^{-1}).

Impurity and umklapp Scattering Relaxation Times

The relaxation times used to describe the scattering events in a propagon-dominated a-Si system are based on the equation for impurity and umklapp scattering in bulk crystalline silicon:

$$\frac{1}{\tau} = A\omega^4 + BT\omega^2 \exp\left(-\frac{C}{T}\right) \tag{S6}$$

where τ is the relaxation time. The first term in Eq. S6 describes impurity scattering, while the second term describes umklapp scattering. Normal scattering is not included since we are experimenting at room temperature; at temperatures, T, such that $T \geq 0.1\theta_D$, where θ_D is the Debye temperature, umklapp scattering dominates over normal scattering such that normal scattering can be neglected[11]. The thermal conductivity of bulk crystalline silicon can be calculated using a kinetic theory model:

$$\kappa_{Si} = \frac{1}{3}\sum_j \int_0^{\omega_{max,j}} \hbar\omega D_j(\omega)\frac{\partial f}{\partial T} v_j^2 \tau_j d\omega \tag{S7}$$

where j is an index that refers to the polarization (longitudinal or transverse, ω_{max} is the maximum frequency of phonon contribution to thermal conductivity, $\hbar$ is the reduced Plank's constant, ω is the phonon frequency, D is the phonon density of states, f is the phonon equilibrium distribution function (assumed to be Bose-Einstein distribution), and v is the sound speed. Fitting to bulk literature thermal conductivity data sampled over 100 - 700 K using a Debye approximation, we find that A = 1.82x10^{-45} s^3, B = 2.8x10^{-19} s K^{-1}, and C = 182 K. Figure S6 shows the data and fit using this approach. We note that for the film thicknesses used in the study, impurity and umklapp scattering contribute little to the overall scattering time compared with the boundary scattering term when applied to our propagon thermal conductivity model. Removing these scattering term and leaving only the boundary scattering term, we find that

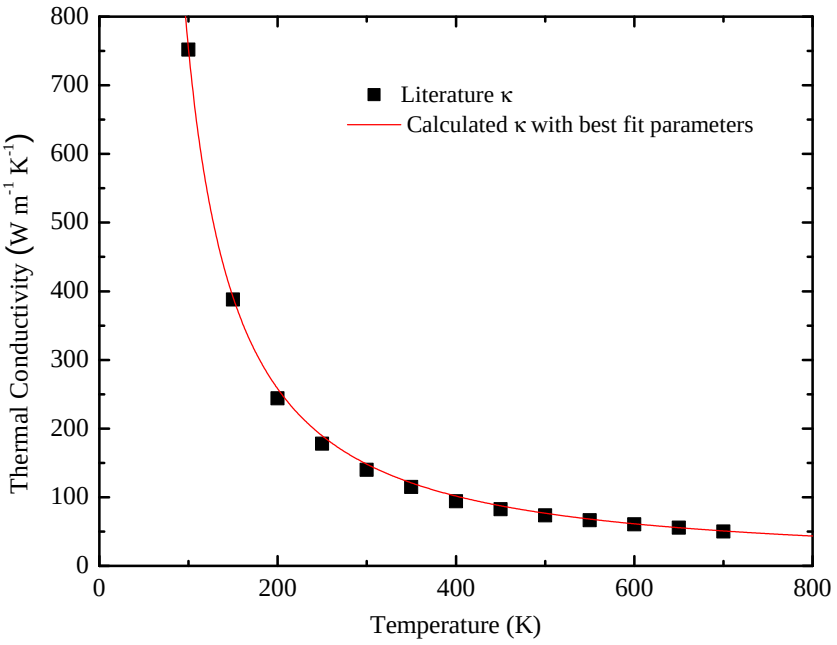

Figure S6: Bulk thermal conductivity of crystalline silicon and model using best fit parameters

our $f_{p\to d}$ as calculated via Eq. 3 is 1.70 THz instead of the 1.82 THz calculated when including these terms.

Total Thermal Conductivity Model

Our model for total thermal conductivity is described by the sum of contributions to thermal conductivity from diffusons and propagons:

$$\kappa_{a-Si} = \kappa_{\text{diffuson}} + \frac{1}{3}\sum_{j}\int_{0}^{\omega_{p\to d,j}} \hbar\omega D_j(\omega)\frac{\partial f}{\partial T}v_j^2\tau_j d\omega \tag{S8}$$

where $\omega_{p\to d}$ is the crossover angular frequency (from propagon regime to diffuson regime) and ω is the propagon angular frequency. This model assumes that the diffuson thermal conductivity (κ_{diffuson}) is constant as a function of film thickness given that, by definition, diffusons have mean free paths on the order of interatomic spacing. With this model, we capture our data with a best fit value for $f_{p\to d}$ of 1.82 THz. To validate this result, we repeat this procedure using only the directly measured data and assuming that κ_{diffuson} is described by the minimum thermal conductivity model, such that $\kappa_{\text{diffuson}} = 1.0$ W m^{-1} K^{-1}. In this case, we fit a value for $f_{p\to d}$ of 1.87 THz, in close agreement with our initial result.

Molecular Dynamics: a-Si Thermal Conductivity in a c-Si/a-SiO_2/a-Si System

We performed molecular dynamics simulations of the c-Si/a-SiO_2/a-Si system to investigate the trend of a-Si thermal conductivity with thickness. Figure S7 shows a schematic of the system. All simulations were performed in LAMMPS [12], had boundaries periodic in the x and y directions, used a time step of 0.5 fs, and used a Tersoff potential for atomic interactions [13] with a modified form of the cutoff function [14]. Domain creation consisted of two steps: vitrification of a 1 nm native oxide layer [15], and the creation and joining of a-Si of various thicknesses to the c-Si/a-SiO_2 system. Unless otherwise stated, the system was run in the NVT ensemble (constant number, volume, temperature) with temperatures controlled by a Nosé-Hoover thermostat [16, 17] with a coupling time of 1 ps. Three system geometries were investigated. In geometry A, the initial system consisted of 5×5×200 unit cells of c-Si, capped by 5×3×1.22 unit cells of strained SiO_2 in the tridymite phase, with the c-axis parallel to c-Si [001]. The c-Si lattice constant was set to 5.43097 Å, causing a compressive strain of about −0.004 at 300 K.

The SiO_2 was heated to 4500 K for 100 ps while the c-Si was held at 300 K. The SiO_2 was then quenched at 10 K/ps back to 300 K. Separate from the c-Si/SiO_2 system, a 5×5×N unit cell block of Si (N–7=9, 15, 23, 37, 58, 146[1]) was heated from 300 K to 4500 K over 50 ps, held at 4500 K for 75 ps, then quenched to 300 K at 10 K/ps. The newly formed a-Si was then joined to the c-Si/a-SiO_2 by placing the two domains spatially adjacent to each other and giving the a-Si a velocity of 0.1 Å/ps towards the c-Si/a-SiO_2. During the joining, the whole system was annealed at 2000 K for 200 ps and the system momentum was zeroed every 10 ps after 40 ps had passed to minimize undesired acoustic oscillations. After annealing, the system was re-cooled to 300 K at 10 K/ps. Finally, the whole system was equilibrated for 100 ps with an imposed temperature profile close to that expected for the steady state of the non-equilibrium measurement of thermal conductivity. That is, the c-Si portion was kept at 300 K and the a-SiO_2 and a-Si portions had a linear temperature gradient from 300 K to 340 K imposed on them by a Langevin thermostat [18] with a coupling time of 1 ps.

System geometries B and C explored size effects other than the thickness. In geometry B, the dependence of thermal conductivity on total system length, not just a-Si thickness, was investigated by setting the c-Si and a-Si thicknesses to 151 and 58 unit cells, respectively. This gave the system a total length equal to the 9 unit cell geometry A simulation. In geometry C, the effect of the cross-sectional dimensions was investigated by setting the c-Si and a-Si thicknesses to 40 and 58 unit cells, respectively, and the cross-sectional dimensions to 6 and 8 unit cells. In this case, the a-SiO_2 was formed from a 6×5×1.22 unit cell block of strained tridymite-SiO_2.[2]

After the domain creation, data were collected with the following procedure. End walls were imposed on both sides and a 2×2 array of cones with radii of 0.68 nm and height 2.72 nm were made by immobilizing atoms to mitigate undesired size effects (Figure S7) [19]. The 2 nm thick cold and hot baths maintained temperatures of 300 K and 340 K, respectively, using a Langevin thermostat [18] with a coupling time of 1 ps. The Langevin thermostat is

[1] The N–7 term accounts for the wall and cones, see following paragraph

[2] The cone radii were adjusted to form a 3×4 array of cones, see following paragraph.

effective at re-thermalizing phonons, also mitigating size effects [20]. Data were collected over 4.5 ns (L≤31.5 nm) or 9.5 ns (L=79.3 nm) in the NVE ensemble (constant number, volume, energy), followed by 25×2^{16} times steps (819 ps) during which the atomic velocities were sampled every 25 time steps to calculate the vibrational density of states within several 1 nm thick slabs located within the bulk c-Si and a-Si, and close to the interface. Steady state was achieved within 200 ps after the baths were imposed. The heat flux was calculated from the energy added to and removed from the baths. The temperature profile was obtained by partitioning the domain into 1 nm bins and recording the bin temperatures every 100 time steps.

Five independent systems were generated for each a-Si thickness and domain geometry, and the thermal conductivity was calculated from $k = -q/\nabla T$. The density of states was calculated as:

$$g(\omega) = \frac{2}{k_B T V t_f} \sum_{i,\alpha} m_i |\mathcal{F}\left[\dot{u}_{i,\alpha}(t)\right]|^2 \tag{S9}$$

where ω is angular frequency, k_B is Boltzmann's constant, T is temperature, V is the slab volume, t_f is the duration of data collection (819 ps), m_i and $\dot{u}_i$ are the mass and velocity of atom i, α indexes the cartesian directions, and $\mathcal{F}$ is the Fourier transform defined as: $\mathcal{F}[h(t)] \equiv \int_{-\infty}^{\infty} h(t)\exp(-i\omega t)\mathrm{d}t$. The density of states were averaged across the five trials and then smoothed by a Gaussian filter with a standard deviation of 0.01 THz.

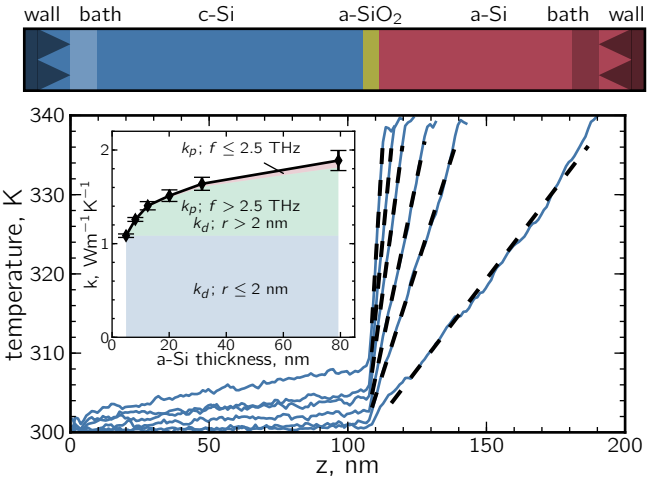

Figure S7: Simulation domain schematic (not to scale) and time-averaged steady-state temperature profiles from one trial for each thickness (geometry A). Dashed lines denote regions where ∇T was measured to obtain k. Inset shows the corresponding thickness-dependent thermal conductivity and the estimated contribution of propagon and diffuson populations.

Figure S7 presents the temperature profiles and thickness-dependent thermal conductivity of geometry A. The thermal conductivity of a-Si is too low to resolve the thermal boundary conductance of the c-Si/a-SiO_2/a-Si interface.

The strain of about -0.004 has a negligible effect on the thermal conductivity compared to an unstrained system [21]. The thermal conductivity of geometry B was 1.64 ± 0.09 $\mathrm{Wm^{-1}K^{-1}}$, the same as geometry A for the same a-Si thickness. Thus, the calculated thermal conductivity depends only on the a-Si thickness. The thermal conductivity of geometry C was 1.63 ± 0.04 $\mathrm{Wm^{-1}K^{-1}}$, so the effect of the cross-section is negligible for dimensions on the order of a few nanometers.

We roughly estimate the contribution by propagons and diffusons of different frequencies and length-scales to the thermal conductivity as plotted in Figure S7. The contribution by propagons with frequencies below 2.5 THz (red) is calculated by Equation S20 with v_T and v_L equal to 3.9 and 7.9 nm/ps, respectively, and the same scattering coefficients as used in Equation S19. The density of states shows that all modes below 2.5 THz are propagons (Figure S8). The smallest a-Si thickness studied was 5 nm. Since diffusons transmit energy by the coupling of adjacent modes, only modes with a characteristic length scale, or radius r, of roughly 2 nm or less can contribute to the thermal conductivity of 5 nm a-Si, and this contribution (blue) should remain constant with a-Si length. As the a-Si becomes thicker, diffuson modes with larger radii may contribute, along with any propagons that are present above 2.5 THz (green). The initial rise in the total thermal conductivity is therefore likely due to larger scale diffuson modes becoming accessible as the sample lengthens. Prior simulation results show that the participation ratio of diffuson modes can remain significant out to 2 nm [22]. Over the whole thickness range, the contribution of low-frequency propagons increases as their mean-free-paths lengthen. Thicknesses greater than 80 nm become difficult to simulate due to the time scales accessible to simulations.

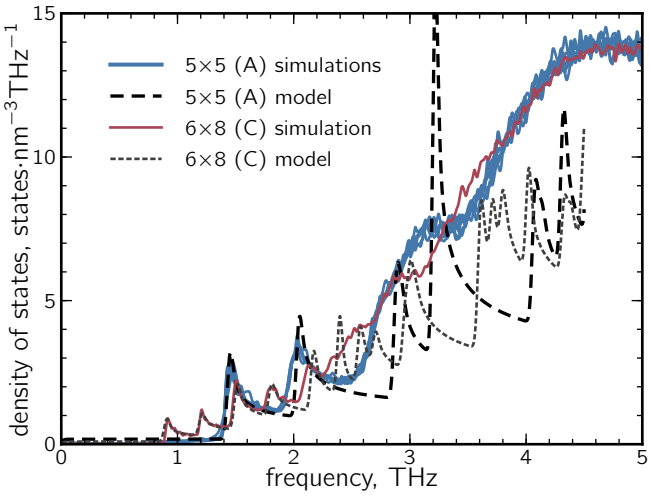

Figure S8: Density of states calculated from simulation for geometries A and C having cross-sections of 5×5 and 6×8 unit cells, respectively. The data are compared to a theoretical model given by Equation S13.

The density of states for geometries A and C are presented in Figure S8. The two curves overlap above about 4 THz; any effect due to the cross-sectional

dimension therefore occur below 4 THz. The data for geometry A below about 2.5 THz is well fit by a quasi-1D model (Equation S13), in agreement with the propagon-diffuson crossover of 2.4 THz for a-Si calculated by Allen *et al.* [22]. The first and second peaks are due to transverse propagons with a sound speed of 3.9 nm/ps and integral wavenumbers $(n_x,n_y) = (\pm1,0)$ or $(0,\pm1)$ and $(\pm1,\pm1)$, respectively. The data and model for geometry C begin to diverge at about 2.0 THz. It is possible that as the cross-sectional dimensions are increased, the cross-over frequency would approach a finite constant that agrees with the experiment. Even so, the low frequency trend in the simulated density of states markedly differs from the 3-D Debye density of states, indicating that the size effects exhibited in the molecular dynamics simulation should not be assumed to have the same form as in experiment.

The quasi-1D density of states exhibited in these simulations will matter most for simulations of glasses and alloys, where the low frequency energy carriers may contribute a significant amount to the total thermal conductivity. Such simulations may not recreate the vibrational physics relevant to transport in the experimental system. Furthermore, the cross-sectional dimensions of about 2.7 nm for geometry A are less than the effective radius of many extended diffuson modes [22], which might introduce additional size effects into the diffuson population which would not be present in the experimental system. Nevertheless, the a-Si thermal conductivity exhibits a clear length dependence up to the thickest samples investigated (Figure S7). One notes, however, that this increase becomes less significant as film thickness increases, such that thermal conductivity (specifically the contribution from diffusons) shows an asymptopic trend as film thickness increases.

We caution that the MD-predicted thermal conductivities for amorphous materials depend on the sample preparation method such as the melt-quench procedure and annealing time implemented during sample preparation. To this end, we have conducted additional NEMD simulations on isolated amorphous Si (with thicknesses similar to those used for the system geometries reported above) prepared after annealing at 1100 K for 10 ns. This results in the removal of metastability as evident from the decrease and plateau in the sample potential energy. Further, we use a relatively slower quench rate of 0.3 K/ps during our sample preparation. The thermal conductivities for the structures prepared with this procedure are slightly lower than those reported for the above geometries, however, the trends in the increase in thermal conductivity with sample thickness remains unchanged.

Quasi One Dimensional Density of States

In this section we derive the phonon density of states for a quasi one dimensional system, for which the wavenumbers in the x and y directions may only take on discrete values. The number of states between k_z and $k_z + \mathrm{d}k_z$ for a true one dimensional system is:

$$N(k_z) = 2\frac{L}{2\pi}\mathrm{d}k_z \tag{S10}$$

where k_z is the wavevector in the one direction permitted in the one dimensional system, and L is the length of the system. Now, expanding the one dimensional system in the cross-sectional direction so that the x and y boundaries are periodic and not too long, the Debye approximation gives a phonon dispersion:

$$\omega = v_j\sqrt{k_x^2 + k_y^2 + k_z^2} \tag{S11}$$

where v_j is the group velocity of the j^{th} polarization. Because of the periodic boundaries, k_x may only take on values of $2\pi n_x/L_x$, where n_x is an integer and L_x is the length of the system in the x direction, and likewise for k_y. The number of states between ω and $\omega + \mathrm{d}\omega$ is thus:

$$N(\omega) = \frac{L}{\pi}\frac{\omega}{v_j^2}\left[\frac{\omega^2}{v_j^2} - \left(k_x^2 + k_y^2\right)\right]^{-\frac{1}{2}}\mathrm{d}\omega \tag{S12}$$

Normalizing by the system volume and the frequency interval; summing over n_x, n_y, and j, and noticing that the minimal value of $\omega(k_z)$ is $v_j\sqrt{k_x^2 + k_y^2}$ yields the density of states as:

$$g(\omega) = \frac{1}{\pi L_x L_y}\sum_j\sum_{n_x,n_y}\frac{\omega}{v_j^2}\left[\frac{\omega^2}{v_j^2} - \left(k_x^2 + k_y^2\right)\right]^{-\frac{1}{2}}\mathcal{H}\left(\omega - v_j\sqrt{k_x^2 + k_y^2}\right) \tag{S13}$$

where $\mathcal{H}(\xi)$ is the Heaviside function.

Confined Propagon Thermal Conductivity

The effect of confinement as evidenced by the low frequency density of states (Figure S8) affects the thickness-dependent thermal conductivity as calculated by simulations (Figure S7). The contribution of the low frequency propagons present in the simulation domain may be estimated from a phonon transport calculation approach. We assume that all energy carriers below a certain cutoff frequency are propagons that scatter with a rate that composites propagon-propagon scattering and propagon boundary scattering. We also use a Debye approximation. The heat flux of a quasi one-dimensional system is:

$$J = \frac{1}{L}\sum_j\sum_{n_x,n_y,n_z} v_{j,z}\hbar\omega f \tag{S14}$$

where L is the length of the quasi one-dimensional system, j indexes polarizations, $n_{x,y,z}$ are integers defining the wavevector, v_z is the velocity in the axial

direction, $\hbar$ is the reduced Planck's constant, ω is angular frequency, and f is the phonon occupation. For a true one-dimensional system, there would be only one polarization and n_x and n_y would be restricted to zero.

Converting the sum over n_z to an integral over wavenumber k_z and splitting the integral in two yields:

$$J = \frac{1}{2\pi} \sum_j \sum_{n_x,n_y} \left\{ \int_{-\infty}^{0} v_{j,z} \hbar\omega f_2 \mathrm{d}k_z + \int_{0}^{\infty} v_{j,z} \hbar\omega f_1 \mathrm{d}k_z \right\} \tag{S15}$$

The left- and righthand integrals account for propagons traveling in the negative and positive z directions, with populations of f_2 and f_1, respectively. The integrals over wavenumber can be converted to integrals over frequency using the Debye dispersion:

$$\mathrm{d}k_z = \frac{|\mathbf{k}|}{v_j k_z} \mathrm{d}\omega. \tag{S16}$$

Since $v_{j,z} = v_j \frac{k_z}{|\mathbf{k}|}$, Equation S15 becomes:

$$J = \frac{1}{2\pi} \sum_j \sum_{n_x,n_y} \left\{ \int_{\omega_{max}}^{\omega_{min}} \hbar\omega f_2 \mathrm{d}\omega + \int_{\omega_{min}}^{\omega_{max}} \hbar\omega f_1 \mathrm{d}\omega \right\} \tag{S17}$$

where $\omega_{min} = v_j \sqrt{k_x^2 + k_y^2}$.

From kinetic theory [23], the difference in population between propagons traveling in the positive and negative directions having the same frequency is, within a linear approximation, given by:

$$f_1 - f_2 = -\tau v_z \frac{\partial f_0}{\partial T} \frac{\partial T}{\partial z} \tag{S18}$$

where f_0 is the equilibrium propagon distribution given by the Boltzmann distribution for classical molecular dynamics. The relaxation time, τ, is modeled having contributions from boundary scattering and propagon-propagon scattering:

$$\tau = \left[\frac{2v_z}{L} + AT\omega^2 \exp\left(-\frac{B}{T}\right) \right]^{-1} \tag{S19}$$

Finally, plugging Equation S18 into Equation S17, normalizing by the domain's cross-sectional area, and comparing to Fourier's Law yields the final result:

$$k_{\mathrm{prop}} = \frac{1}{2\pi L_x L_y} \frac{\hbar^2}{k_B T^2} \sum_j \sum_{n_x,n_y} \int_{v_j\sqrt{k_x^2+k_y^2}}^{\omega_{max}} \omega \exp\left(-\frac{\hbar\omega}{k_B T}\right) \left[\frac{\omega^2}{v_j^2} - \left(k_x^2 + k_y^2\right) \right]^{\frac{1}{2}} v_j^2 \tau \mathrm{d}\omega \tag{S20}$$

where $k_{x,y} = 2\pi n_{x,y}/L_{x,y}$, L_x and L_y are the cross-sectional dimensions and k_B is Boltzmann's constant.

References

[1] Tomoko Sato, Nobumasa Funamori, and Takehiko Yagi. Helium penetrates into silica glass and reduces its compressibility. *Nat Commun*, 2:345, 06 2011. URL http://dx.doi.org/10.1038/ncomms1343.

[2] Frank L. Galeener. Band limits and the vibrational spectra of tetrahedral glasses. *Phys. Rev. B*, 19:4292–4297, Apr 1979. doi: 10.1103/PhysRevB.19.4292. URL http://link.aps.org/doi/10.1103/PhysRevB.19.4292.

[3] F. L. Galeener, R. A. Barrio, E. Martinez, and R. J. Elliott. Vibrational decoupling of rings in amorphous solids. *Phys. Rev. Lett.*, 53:2429–2432, Dec 1984. doi: 10.1103/PhysRevLett.53.2429. URL http://link.aps.org/doi/10.1103/PhysRevLett.53.2429.

[4] Dionisio Bermejo and Manuel Cardona. Raman scattering in pure and hydrogenated amorphous germanium and silicon. *Journal of Non-Crystalline Solids*, 32(1–3):405 – 419, 1979. ISSN 0022-3093. doi: http://dx.doi.org/10.1016/0022-3093(79)90085-1. URL http://www.sciencedirect.com/science/article/pii/0022309379900851. Electronic Properties and Structure of Amorphous Solids.

[5] M. H. Brodsky, Manuel Cardona, and J. J. Cuomo. Infrared and raman spectra of the silicon-hydrogen bonds in amorphous silicon prepared by glow discharge and sputtering. *Phys. Rev. B*, 16:3556–3571, Oct 1977. doi: 10.1103/PhysRevB.16.3556. URL http://link.aps.org/doi/10.1103/PhysRevB.16.3556.

[6] F. L. Galeener and G. Lucovsky. Longitudinal optical vibrations in glasses: Geo_2 and sio_2. *Phys. Rev. Lett.*, 37:1474–1478, Nov 1976. doi: 10.1103/PhysRevLett.37.1474. URL http://link.aps.org/doi/10.1103/PhysRevLett.37.1474.

[7] Z Iqbal and S Veprek. Raman scattering from hydrogenated microcrystalline and amorphous silicon. *Journal of Physics C: Solid State Physics*, 15(2):377, 1982.

[8] J. S. Lannin, L. J. Pilione, S. T. Kshirsagar, R. Messier, and R. C. Ross. Variable structural order in amorphous silicon. *Phys. Rev. B*, 26:3506–3509, Sep 1982. doi: 10.1103/PhysRevB.26.3506. URL http://link.aps.org/doi/10.1103/PhysRevB.26.3506.

[9] Ruxandra M. Costescu, Marcel A. Wall, and David G. Cahill. Thermal conductance of epitaxial interfaces. *Phys. Rev. B*, 67:054302, Feb 2003. doi: 10.1103/PhysRevB.67.054302. URL http://link.aps.org/doi/10.1103/PhysRevB.67.054302.

[10] S.-M. Lee and David G. Cahill. Heat transport in thin dielectric films. *Journal of Applied Physics*, 81:2590, 1997.

[11] Glen A. Slack and S. Galginaitis. Thermal conductivity and phonon scattering by magnetic impurities in cdte. *Phys. Rev.*, 133:A253–A268, Jan 1964. doi: 10.1103/PhysRev.133.A253. URL http://link.aps.org/doi/10.1103/PhysRev.133.A253.

[12] Steve Plimpton. Fast parallel algorithms for short-range molecular dynamics. *Journal of Computational Physics*, 117(1):1 – 19, 1995. ISSN 0021-9991. doi: http://dx.doi.org/10.1006/jcph.1995.1039. URL http://www.sciencedirect.com/science/article/pii/S002199918571039X.

[13] Shinji Munetoh, Teruaki Motooka, Koji Moriguchi, and Akira Shintani. Interatomic potential for si–o systems using tersoff parameterization. *Computational Materials Science*, 39(2):334 – 339, 2007. ISSN 0927-0256. doi: http://dx.doi.org/10.1016/j.commatsci.2006.06.010. URL http://www.sciencedirect.com/science/article/pii/S0927025606002023.

[14] T. Kumagai, S. Izumi, S. Hara, and S. Sakai. Development of bond-order potentials that can reproduce the elastic constants and melting point of silicon for classical molecular dynamics simulation. *Computational Materials Science*, 39(2):457 – 464, 2007. ISSN 0927-0256. doi: http://dx.doi.org/10.1016/j.commatsci.2006.07.013. URL http://www.sciencedirect.com/science/article/pii/S0927025606002254.

[15] Yuhai Tu and J. Tersoff. Structure and energetics of the si- sio_2 interface. *Phys. Rev. Lett.*, 84:4393–4396, May 2000. doi: 10.1103/PhysRevLett.84.4393. URL http://link.aps.org/doi/10.1103/PhysRevLett.84.4393.

[16] Shuichi Nosé. A unified formulation of the constant temperature molecular dynamics methods. *The Journal of Chemical Physics*, 81(1):511–519, 1984. URL http://scitation.aip.org/content/aip/journal/jcp/81/1/10.1063/1.447334.

[17] William G. Hoover. Canonical dynamics: Equilibrium phase-space distributions. *Phys. Rev. A*, 31:1695–1697, Mar 1985. doi: 10.1103/PhysRevA.31.1695. URL http://link.aps.org/doi/10.1103/PhysRevA.31.1695.

[18] T. Schneider and E. Stoll. Molecular-dynamics study of a three-dimensional one-component model for distortive phase transitions. *Phys. Rev. B*, 17:1302–1322, Feb 1978. doi: 10.1103/PhysRevB.17.1302. URL http://link.aps.org/doi/10.1103/PhysRevB.17.1302.

[19] Zhi Liang and Pawel Keblinski. Finite-size effects on molecular dynamics interfacial thermal-resistance predictions. *Phys. Rev. B*, 90:075411, Aug 2014. doi: 10.1103/PhysRevB.90.075411. URL http://link.aps.org/doi/10.1103/PhysRevB.90.075411.

[20] K. Sääskilahti, J. Oksanen, J. Tulkki, and S. Volz. Role of anharmonic phonon scattering in the spectrally decomposed thermal conductance at planar interfaces. *Phys. Rev. B*, 90:134312, Oct 2014. doi: 10.1103/PhysRevB.90.134312. URL http://link.aps.org/doi/10.1103/PhysRevB.90.134312.

[21] Kevin D. Parrish, Ankit Jain, Jason M. Larkin, Wissam A. Saidi, and Alan J. H. McGaughey. Origins of thermal conductivity changes in strained crystals. *Phys. Rev. B*, 90:235201, Dec 2014. doi: 10.1103/PhysRevB.90.235201. URL http://link.aps.org/doi/10.1103/PhysRevB.90.235201.

[22] Philip B. Allen, Joseph L. Feldman, Jaroslav Fabian, and Frederick Wooten. Diffusons, locons, propagons: Character of atomic vibrations in amorphous si. *Philosophical Magazine B*, 79:1715, 1999.

[23] Gang Chen. *Nanoscale Energy Transport and Conversion: A Parallel Treatment of Electrons, Molecules, Phonons, and Photons.* Oxford University Press, USA, 2005.